

Contents lists available at ScienceDirect

Combustion and Flame

journal homepage: www.sciencedirect.com/journal/combustion-and-flame





Large eddy simulation of plasma assisted ignition: Effects of pulse repetition frequency, number of pulses, and pulse energy

Taaresh Sanjeev Taneja a, Timothy Ombrello b, Joseph Lefkowitz c, Suo Yang a,*

- ^a Department of Mechanical Engineering, University of Minnesota Twin Cities, Minneapolis, MN 55455, USA
- b Aerospace Systems Directorate, U.S. Air Force Research Laboratory, Wright-Patterson AFB, OH 45433, USA
- ^c Faculty of Aerospace Engineering, Technion Israel Institute of Technology, Haifa 3200003, Israel

ARTICLE INFO

Keywords: Plasma assisted combustion Nanosecond repetitively pulsed plasma Pulse repetition frequency (PRF) Ignition Kernel development

ABSTRACT

The impacts of the pulse repetition frequency (PRF), number of pulses, and energy per pulse in a train of nanosecond discharge pulses on the ignition of a flowing lean premixed methane-air mixture are investigated using numerical simulations. A phenomenological plasma model coupled with a compressible reacting flow solver is used for these simulations. The simulation strategy has been well validated by comparing the experimental schlieren and OH planar laser induced fluorescence (PLIF) results with the numerical schlieren (i.e., density gradient) and OH density profiles, respectively. The characteristics of the ignition kernels produced by each discharge pulse and their interaction with each other as functions of the PRF are investigated. Three regimes were defined in the literature based on this interaction of the ignition kernels — fully coupled, partially coupled, and decoupled. This study uses numerical simulations to probe into the constructive and destructive effects, that ultimately determine ignition success, in these different regimes. The complete overlap of kernels and the complete lack of synergy between kernels produced by consecutive pulses are attributed to the success and failure of ignition and flame propagation in the fully coupled and decoupled regimes, respectively. In the partially coupled regime, the convection heat loss driven by the shock-turned-acoustic wave of the next discharge pulse, on the kernel produced by the previous discharge pulse, in addition to diffusion losses, contribute to ignition failure. However, the expansion of the next kernel in a region of higher average temperature and radical concentration created by the previous kernel could help to bridge the gap between the two kernels and result in successful ignition. The important parameters of energy per pulse, number of pulses, and equivalence ratio affect the competition between these constructive and destructive effects, which eventually determines the ignition success in this regime. Finally, the change in the nature of interaction between consecutive kernels from decoupled to partially coupled, at the same frequency but with different energies per pulse, is also shown.

Novelty and significance statement

This study presents large eddy simulation (LES)-based results on the impact of the pulse repetition frequency (PRF), number of pulses, and energy per pulse, on the success of plasma assisted ignition of a flowing lean premixed methane-air mixture. This is the first simulation work to show direct validation based on both schlieren and OH density from the experiments of Lefkowitz et al. (2021). This is also the first work which identifies and explains the constructive and destructive effects to explain the reduced ignition probability in the partially coupled regime observed in Lefkowitz and Ombrello (2017). The role of the shock-turned-acoustic wave produced by every subsequent discharge pulse, on the previous kernel in a pulse train (destructive); and the assistance provided by the previous kernel to the next kernel (constructive), has been shown quantitatively. The use of a compressible solver is imperative to identify this destructive effect. The change in the regime boundaries defined by the PRF, by changing the energy deposition, is also shown.

1. Introduction

Thermal plasma, often called thermal arcs, have been the most common sources used for ignition of fuel-air mixtures in reciprocating

engines, gas turbines, rocket combustors and scramjets. This is mainly because of the intense heat that they locally produce, which can trigger

E-mail address: suo-yang@umn.edu (S. Yang).

https://doi.org/10.1016/j.combustflame.2024.113574

Received 3 March 2024; Received in revised form 17 June 2024; Accepted 17 June 2024 Available online 3 July 2024

0010-2180/© 2024 The Combustion Institute. Published by Elsevier Inc. All rights are reserved, including those for text and data mining, AI training, and similar technologies.

Corresponding author.

ignition [1]. In contrast, non-equilibrium plasma offers the benefits of ultra-fast gas heating as well as production of reactive radicals due to various additional chemical pathways created due to the excitation (and quenching) and ionization (and recombination) of the reactants. Moreover, even though the energy from non-equilibrium plasma for ignition might be low, the rates of energy deposition can be very high, especially since most non-equilibrium plasmas for ignition are produced using nanosecond high-voltage pulses, which are cutoff before they transition to a thermal arc. Furthermore, the mechanisms of ultra-fast gas heating (primarily associated with energy release due to quenching of electronic excited states of N2 in air at nanosecond timescales) and radical formation are primarily driven by the electron impact kinetics and the following relaxation of excited states of certain species [2] in non-equilibrium plasma, which is very different from the direct increase of kinetic energy of gas molecules (i.e., direct heating) in thermal (equilibrium) plasma. Thus, non-equilibrium plasma offers more operating parameters, such as the voltage profile and duration, electrode geometry and inter-electrode gap distance, and pulse repetition frequency (PRF), to control the rates of these kinetic processes, which can result in different regimes of plasma [3] and varied chemical and gas heating pathways. In addition to the source parameters, the gas composition (equivalence ratio), temperature, pressure and background flow also affect the plasma regime and the overall characteristics of the plasma, particularly for the applications to ignition and flame stabilization. Lefkowitz, Ombrello, and their co-workers performed various experiments of nanosecond pulsed high frequency discharge (NPHFD)based ignition in their subsonic ignition tunnel facility and reported qualitative and quantitative analyses in their papers [4-7].

Lefkowitz et al. [6] discussed the impact of the pulse repetition frequency on the OH radical production rates (using OH planar laser induced fluorescence, PLIF) and evolution of the ignition kernel (using schlieren imaging). They showed how pulse repetition frequencies (PRF) greater than 10 kHz result in accumulation of OH radicals which eventually assists in sustained ignition kernel formation and increasing the ignition probability. A wider parametric exploration investigating the effect of operating conditions, such as the inter-pulse time, number of pulses, gap distance, equivalence ratio, and flow velocity, on the ignition kernel development rate in NPHFD ignition was presented in Lefkowitz and Ombrello [5]. They concluded that increasing the interpulse time resulted in faster ignition kernel volume growth rate for a constant total energy deposition, as long as the kernel growth is still in the fully coupled regime, which is characterized by complete overlap of high-temperature and radical-rich hot-spots produced by successive discharge pulses. They also found that increasing the number of pulses reduced the time to form a self-sustained ignition kernel at a fixed PRF. Moreover, it was reported that reducing the inter-electrode gap distance increased local quenching which inhibited growth of the ignition kernel. This was attributed to the faster rates of heat transfer and radical loss at the electrode surfaces, for smaller inter-electrode gaps. An interesting observation reported in Lefkowitz and Ombrello [4] was the non-monotonic dependence of ignition probability on the pulse repetition frequency. The authors performed ignition experiments in their subsonic ignition tunnel configuration with pin-pin electrodes, in the pulse repetition frequency range of 1-300 kHz. They categorized the evolution trends of the kernels represented by the ignition probability into three regimes, based on the pulse repetition frequency, namely the fully coupled regime (> 7 kHz), the partially coupled regime (2-7 kHz), and the decoupled regime (< 2 kHz). Multiple experiments performed with different number of pulses at a fixed flow velocity, equivalence ratio, and gap distance showed a significant decrease in the ignition probability in the partially coupled regime. This probability was even lower than that in the decoupled regime where the kernels develop independently, which seems counter-intuitive. The numerical simulation results presented in this work provide important physical insights, which can help in explaining this anomalous non-monotonic behavior observed in experiments. Similar tests were also performed

in Lefkowitz and Ombrello [4] by varying the inter-electrode gap distance and holding all the other parameters constant. Furthermore, Shen et al. [8] explored the impact of per-pulse energy deposition with varying the pulse repetition frequencies. They concluded that high frequency, low-energy discharges would be an optimal ignition strategy for plasma assisted combustion in terms of ignition energy efficiency and ignition probability.

Given the vastly disparate length and time-scales in plasma assisted combustion, researchers have devised various methods to simulate ignition and flame stabilization with non-equilibrium plasma in a computationally efficient manner. While detailed chemical kinetic studies such as those performed in Refs. [9-13] are used to understand the chemical pathways which uncover the benefits of non-equilibrium plasma for combustion, these studies are restricted to 0D simulations which ignore the flow dynamics and require the electric field as a model input. More detailed works which perform self-consistent modeling of plasma assisted combustion and pyrolysis in 1D, 2D, and 3D, such as Refs. [14-20], are limited in their ability to resolve/model the turbulent reacting flow leading to ignition in a practical environment with both local and bulk transport. Phenomenological modeling of plasma is a compromised approach which aims to only model the most important effects of the non-equilibrium plasma on the turbulent reacting flows in 2D/3D, without solving for the number densities of electrons, ions and excited states and the electric field. One such model was first proposed by Castela et al. [21] where ultra-fast gas heating, O radical production and slow vibrational-translational relaxation were assumed to be the dominant plasma effects. This model was later implemented in OpenFOAM-6 by Taneja and Yang [22]. The current research uses this phenomenological model proposed by Castela et al. [21,23] to model plasma assisted ignition of lean premixed, turbulent flowing mixtures of CH₄-air. Preliminary simulation results of ignition with a single pulse in quiescent and flowing environments and with multiple pulses in fully-coupled and decoupled regimes, at different equivalence ratios were presented in Taneja and Yang [24]. Recently, Bechane and Fiorina [25] also used this model to simulate Lefkowitz and Ombrello's experimental configurations [6]. They were able to show how reducing the background flow velocity and increasing the PRF helped in achieving ignition. They also presented a dimensionless analysis which helped differentiate the fully coupled and decoupled regimes based on inputs such as the flow velocity, discharge diameter, and PRF. They also presented a detailed LES-based analysis using Castela et al.'s plasma model [21], where they compared the evolution of the number of pixels with a detectable OH PLIF signal with the experimental values. However, they used a low Mach solver, which could not capture shock waves and shock-turned-acoustic waves, after every discharge pulse. As a result, an important phenomena leading to the destructive interaction of kernels in the partially coupled regime, which will be discussed in Section 3.2, could not be captured in their research. Furthermore, they focused on the effect of the flow velocity and PRF, whereas the current work focuses on the impact of the PRF, number of pulses, and energy deposition per pulse on the success of ignition, especially in the partially coupled regime.

This paper is structured as follows. Section 2 provides details of the governing equations, numerical schemes, turbulence model, and the phenomenological plasma model used for this computational study. The results of simulation validation by experimental data are also provided at the end of this section. Section 3 presents the simulation results and analysis for the fully coupled, partially coupled, and decoupled cases, which were briefly introduced above. The main emphasis of this work is to probe the effects of pulse repetition frequency, number of pulses and the energy per pulse on the success of ignition and the governing mechanisms of these effects. Finally, the Conclusion Section 4 summarizes all the important findings of this research.

2. Numerical methodology and validation

This section has been divided into three subsections. Section 2.1 presents the governing equations solved in this work, Section 2.2 explains the details of the transonic version of a pressure-based compressible solver and the LES models used for the simulations, and Section 2.3 discusses the numerical setup and the validation case results.

2.1. Governing equations

The phenomenological model proposed by Castela et al. [21] has been implemented and coupled with a transonic pressure-based compressible solver for reacting flows, developed in-house [26,27] on the OpenFOAM-6 platform [28].

Conservation of momentum (Eq. (1)), species mass fractions (Eq. (2)) for all N_{sp} species, total non-chemical enthalpy (Eqs. (3) and (4)) are solved. In Eqs. (1) to (4), ρ is the gas density, u_i is the *i*th component of velocity vector, p is the thermodynamic pressure, τ_{ij} is the ij element of the viscous stress tensor, Y_k is the mass fraction of the kth species, $V_{k,i}$ is the ith component of the diffusion velocity of the kth species in the mixture (calculated using the mixture-averaged model and the Hirschfelder–Curtiss approximation [29]), $\dot{\omega}_k$ is the net production rate of the kth species, W_k is the molecular weight of the kth species, H is the total non-chemical enthalpy of the mixture (Eq. (4)), h_s is average sensible enthalpy of the mixture, $h_{s,k}$ is the sensible enthalpy of the k_{th} species, q_i is the *i*th component of the conduction heat flux, and \dot{Q}_{reac} is the combustion heat release rate. These equations include appropriate source terms for the production of O radicals $(W_O\dot{\omega}_O^P)$, fast gas heating (\dot{E}_{heat}^{p}) , and slow gas heating due to relaxation of vibrational states of N_2 (R_{VT}^p) , from the phenomenological plasma model. In Eq. (2), the total production rate of the kth species has been divided into $\dot{\omega}_{k}^{c}$, the net production rate of species k only due to combustion, and $\dot{\omega}_{k}^{\tilde{p}}$, the net production rate of species k due to the plasma. The closure of these source terms has been listed in Eqs. (6)-(13).

$$\frac{\partial(\rho u_j)}{\partial t} + \frac{\partial(\rho u_i u_j)}{\partial x_i} = -\frac{\partial p}{\partial x_j} + \frac{\partial \tau_{ij}}{\partial x_i} \tag{1}$$

$$\frac{\partial (\rho Y_k)}{\partial t} + \frac{\partial (\rho u_i Y_k)}{\partial x_i} = -\frac{\partial}{\partial x_i} \left(\rho V_{k,i} Y_k \right) + W_k \dot{\omega}_k^c + W_k \dot{\omega}_k^p \tag{2} \label{eq:2}$$

$$\frac{\partial(\rho H)}{\partial t} + \frac{\partial(\rho u_i H)}{\partial x_i} = -\frac{\partial q_i}{\partial x_i} + \frac{\partial(\tau_{ij} u_i)}{\partial x_i} + \frac{\partial p}{\partial t} - \frac{\partial}{\partial x_i} \left(\rho \sum_{k=1}^{N_{sp}} h_{s,k} Y_k V_{k,i} \right) + \dot{Q}_{reac} + \dot{E}_{heat}^p + \dot{R}_{VT}^p$$
(3)

$$H = h_s + \frac{1}{2}u_i u_i \tag{4}$$

Additionally, a transport equation for the vibrational energy density (e_{vib}) is solved, given in Eq. (5) which has a source term, \dot{E}_{vib}^{p} , defined to be a fraction $(1 - \alpha)$ of the total input plasma power density term \dot{E}^p , and a vibrational-translational relaxation sink term, \dot{R}^p_{VT} . \dot{R}_{VT}^{p} is calculated by assuming the Landau–Teller harmonic oscillator model [30] as is done in Millikan and White [31], with the equilibrium value of the vibrational energy, e_{vib}^{eq} , calculated using Eq. (12), and the relaxation timescale, τ_{VT} , evaluated in Eq. (13), as the harmonic mean of timescales associated with relaxation of vibrational states of N2 with collision partners, N₂ (τ_{VT}^{N2}), O₂ (τ_{VT}^{O2}) and O (τ_{VT}^{O}). In Eq. (5), D is the diffusion coefficient of N_2 as the vibrational energy is assumed to be stored only in the vibrational states of N₂. σ_{pulse} and τ_{pulse} in Eq. (6) are the plasma energy density and duration of the pulse (fixed to 50 ns, the experimental value of this pulse duration in [4,6] was 10 ns, however, based on the model assumptions in [21] to match the O radical density rise times, the pulse duration is changed to 50 ns). Model constants a and b used to define the spatial distribution of the plasma power density in Eq. (6) and are set to 6.95×10^{-8} and 2.5, respectively. The fractions of total plasma power density used to generate O radicals (η), and that used in both fast gas heating and O radical production (α) are used to define the net production rate of the O radicals due to the plasma ($\dot{\omega}_p$) in Eq. (7). Furthermore, $Y_{O_2}^f$, e_O , e_{O_2} in Eqs. (7) and (8) refer to the mass fraction of O₂ in the fresh reactants mixture, the enthalpy of formation of O and that of O₂, respectively, and R_u and Θ_1 in Eq. (12) stand for the universal gas constant and equilibrium vibrational temperature of N₂. Detailed discussion on the derivation and usage of Eqs. (7)–(13) can be found in Refs. [21,27]. It should be noted that this model works best when the plasma is in a nanosecond spark phase [3], and when the fuel mass fraction in the mixture is small. In the experiments of Lefkowitz and Ombrello [4], the plasma is indeed in the nanosecond spark phase and all the cases in this work aim to model lean CH₄-air mixtures where the mass fraction of CH₄ is less than 5%. This confirms the applicability of this model, which is fairly detailed yet computationally affordable to perform LES of such multi-time scale applications.

$$\frac{\partial (\rho e_{vib})}{\partial t} + \frac{\partial (\rho u_i e_{vib})}{\partial x_i} = -\frac{\partial}{\partial x_j} \left(\rho D \frac{\partial e_{vib}}{\partial x_i} \right) + \dot{E}^p_{vib} - \dot{R}^p_{VT}$$
 (5)

$$\dot{E}^{p} = \frac{\sigma_{pulse}}{\tau_{pulse}} erfc \left(\frac{r^{2}}{a}\right)^{b} \tag{6}$$

$$\dot{\omega}_{O}^{p} = \eta \frac{Y_{O_{2}}}{Y_{O_{2}}^{f}} \frac{\dot{E}^{p}}{e_{O}}$$

$$\dot{\omega}_{O_{2}}^{p} = -\frac{W_{O}}{W_{O}} \dot{\omega}_{O}^{p}$$
(7)

$$\dot{E}_{chem}^{p} = \frac{\eta Y_{O_2}}{Y_O^f} \left(1 - \frac{W_O e_{O_2}}{W_{O_2} e_O} \right) \dot{E}^p \tag{8}$$

$$\dot{E}_{host}^p = \alpha \dot{E}^p - \dot{E}_{chom}^p \tag{9}$$

$$\dot{E}_{vib}^{p} = (1 - \alpha)\dot{E}^{p} \tag{10}$$

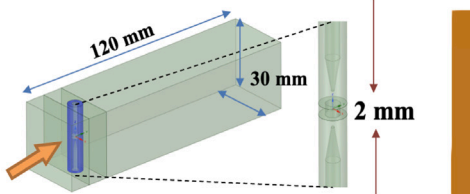
$$\dot{R}_{VT}^{p} = \frac{\rho(e_{vib} - e_{vib}^{eq}(T))}{\tau_{VT}} \tag{11}$$

$$e_{vib}^{eq}(T) = \frac{\frac{R_u}{W_{N_2}}\Theta_1}{\frac{e^{\Theta_1/T} - 1}{e^{\Theta_1/T} - 1}}$$
(12)

$$\tau_{VT} = \left(\frac{1}{\tau_{VT}^{O}} + \frac{1}{\tau_{VT}^{O_2}} + \frac{1}{\tau_{VT}^{N_2}}\right)^{-1} \tag{13}$$

2.2. Reacting flow solver

A pressure-based compressible solver was used instead of a densitybased fully compressible solver, due to the disparate flow timescales of interest in the simulations. The convergence of fully compressible density-based solvers is known to deteriorate at low values of Mach numbers. This slower convergence results from the difference in magnitude between the advective and acoustic wave speeds. The Jacobian of the system of compressible flow equations becomes ill-conditioned at low Mach numbers (i.e., when $c \gg u$), because the ratio of the maximum and minimum eigenvalues (by magnitude) becomes large, which renders the system of equations stiff. This ratio, also called the condition number of a matrix, is $||u + c||/||u|| \approx 1/M$ which becomes very large for small values of Mach number (especially in the low Mach regime). This results in a more restrictive upper bound on the time step size Δt for explicit solvers. The value of Δt is typically of the order of a few tens of microseconds for transonic/supersonic flows, depending on which time stepping scheme is used. And in most scenarios, the actual time-step is smaller than this limit based on the chemical timescales which are usually smaller than the gas dynamics timescales, which typically range from 50–500 ns. However, this Δt can scale to sub-nanoseconds for almost quiescent or low-Mach flows with density-based solvers. For implicit solvers, which implement subcyling,



10 Velocity mag. (m/s)

(a) Computational Domain

(b) Velocity magnitude at the first time step after initialization with the coarse mesh RANS result.

Fig. 1. Computational Domain and initial velocity contour.

this is reflected in the stiffness of the linear system that is solved at each nonlinear iteration.

For the current simulations, the background mean flow of 10 m/s is at a Mach number of ≈ 0.03 , which falls in the low-Mach regime. Furthermore, the local flame displacement speeds observed during the ignition kernel expansion also fall in the low-Mach limit. On the other hand, the current problem features locally transonic flow, because the discharge pulse deposits energy in a very small timescale (e.g., a few nanoseconds). Hence, the typical power densities, which are of the order of 10^{11} – 10^{15} W/m³, create a shock wave (with a shock Mach number of ~ 1.0 –1.2) which then propagates outwards radially and eventually loses energy to the background subsonic flow. This process of the shock wave (a supersonic flow phenomena) turning into a weak compressive acoustic wave (a compressible subsonic flow) happens within a few microseconds, whereas the rest of the flow domain remains in the low-Mach regime. This poses a challenge for traditional density-based and pressure-based solvers. An alternative is to use a pressure-based solver, where the velocity fields are predicted by solving the momentum equations, and the continuity equation is modified to obtain a pressure field, which is then used to correct the velocity field. Thus, a velocity field which satisfies both continuity and momentum equations is obtained after a few iterations when convergence is achieved. The internal energy/enthalpy / temperature equation and the species composition equations are also solved in the same loop, which are then used to evaluate the density using an equation of state. One such algorithm (PISO for compressible flows), which uses operator splitting, has been described in Issa [32]. The current solver uses an extended version of this approach, as is described in Appendix.

Large eddy simulations (LES) using the dynamic Smagorinsky model [33] for the sub-grid scale (SGS) Reynolds stress tensor and the Partially Stirred Reactor (PaSR) model [34] for the SGS filtered chemical source terms have been performed in this work. Verification of the CFD solver [27] was done by comparing 2D DNS results with Castela et al. [21], followed by comparison of kernel development in quiescent and isotropic turbulent environments in a 3D cube, which were compared to results in Castela et al. [23].

2.3. Numerical setup and validation

Similar to Castela et al. [21], the power density is assumed to remain constant with time during the pulse because the energy per pulse used in the experiments remains almost constant after a short initial transient before spark formation occurs. The model constants (i.e., a and b in Eq. (6)) are adjusted based on the inter-electrode gap of 2 mm (as per experiments in [6]) such that the total deposited energy matches a desired input value (2.9 mJ per pulse). In these simulations, the energy fractions for ultra-fast dissociation of O_2 (η), ultra-fast gas heating ($\alpha - \eta$), and ultra-fast vibrational energy increase ($1 - \alpha$) are chosen to be 0.35, 0.20 and 0.45, respectively, same as what was used in Castela et al. [21,23] and also confirmed by our 0D analyses using detailed plasma chemistry.

The cross-sectional dimensions of the subsonic ignition tunnel are 38.1 mm × 38.1 mm, as mentioned in Lefkowitz and Ombrello [4]. In this work, a slightly smaller computational domain has been modeled with cross-sectional dimensions of 30 mm \times 30 mm and a length of 120 mm (shown in Fig. 1(a)). This is because using a smaller domain ensures fewer grid points and obviates the need of high resolution or modeling of the flow near the walls (i.e., wall modeling). This is valid, because the developing ignition kernels are quite far away from the physical boundaries (more than 8 x the average ignition kernel diameter, in each direction) of the domain, and the background flow between and downstream of the inter-electrode gap remains unaffected by walls. Two pin electrodes with a gap distance of 2 mm are located 15 mm downstream of the inlet of the tunnel. The mesh is refined from the domain boundaries to the inter-electrode gap, with the smallest cell size of 12 µm in the inter-electrode gap region. This mesh size can almost completely resolve the heat release zone of a laminar flame (which is ~ 0.1 mm) at the same conditions, as it places ~ 8 points across the heat release zone. The mesh is gradually coarsened up to $25 \mu m$ for a distance of 2 cm downstream of the electrodes, which places 10 points across the flame thickness of the developing ignition kernel and hence is suitable for LES with the partially stirred reactor (PaSR) model [34] used in this work for unresolved turbulence-chemistry interaction. The final mesh comprises of approximately 47 million hexahedral-polyhedral elements. snappyHexMesh is used to perform this successive refinement and create inflation layers near the walls of the electrodes. Subsonic inlet boundary conditions are used at the inlet face and non-reflecting boundary conditions are used at all other faces of the domain to avoid any numerical reflection of acoustic waves off the boundaries. A zero-gradient boundary condition for temperature (i.e., adiabatic), pressure, and mass fractions of all species, and a no-slip boundary condition for velocity are imposed at the electrode walls.

For all simulations, the time step size Δt was fixed at 0.5 ns during each discharge pulse, and was calculated dynamically (ranges from 0.5 ns to 5 μs) based on a maximum CFL number of 0.6 when the discharge pulses are turned off. The fixed value of Δt during the pulse resulted in time-step independent results and a CFL number of up to 0.6 resulted in good computational stability and speed. Second order, total variation diminishing (TVD) central difference approximations were used for the gradient, divergence, and Laplacian terms of all the governing equations. Implicit time integration was done with an Euler scheme. A 30-species reduced GRI-Mech 3.0 [35] was used to compute combustion chemical reaction rates. To ensure accurate estimation of thermodynamic quantities (e.g., specific heat C_p , total enthalpy (H_0) , and total entropy (S_0)) at temperatures as high as 5000 K in some of the simulations, the NASA-7 polynomial coefficients from Goos et al.'s database [36] were used. Thus, the fine grid sizes and time-steps, and the number of variables solved for, resulted in a total computational time of ~6 h for simulating each discharge pulse using 1,280 physical CPU cores of our AMD EPYC 7763 processors. The computational time to simulate the evolution between two discharge pulses depended on the pulse frequency and the degree of stiffness that had been induced by the evolving thermochemical state due to the deposition of the

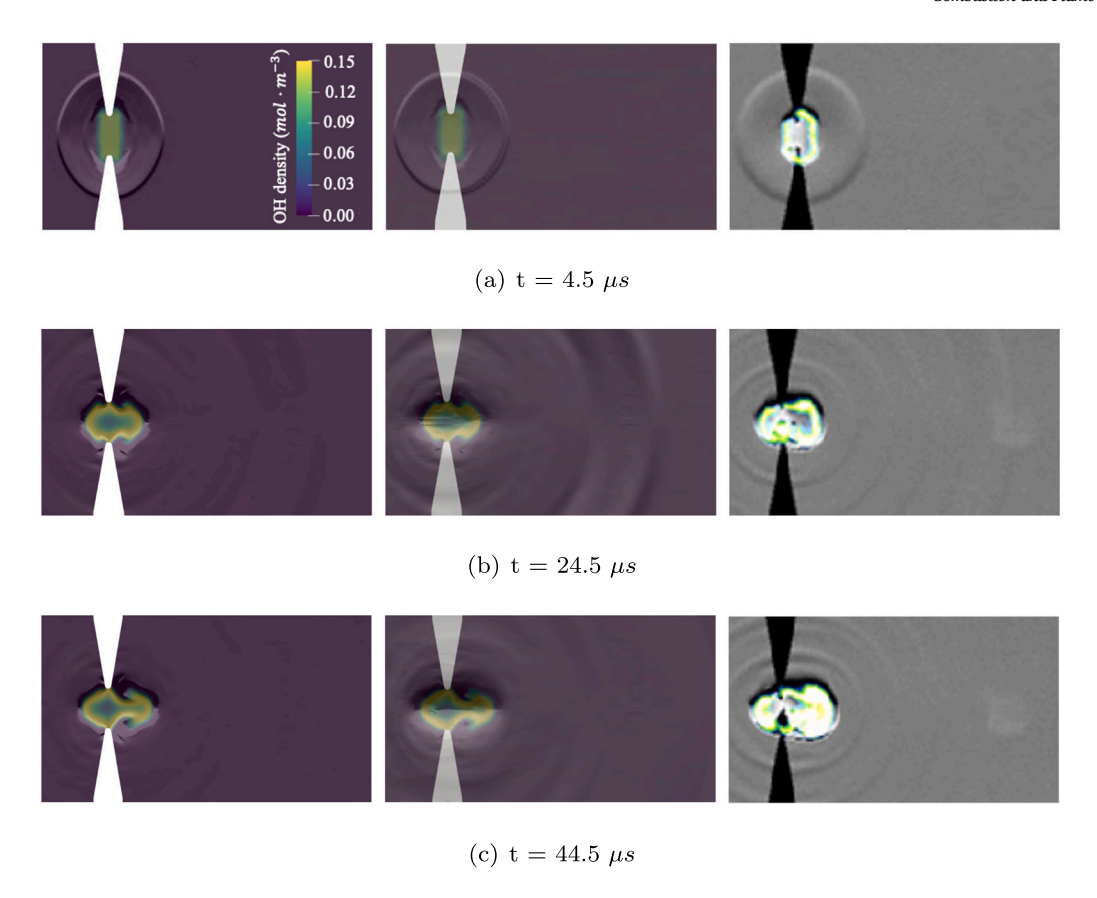


Fig. 2. Computational (OH mass density overlaid on the numerical schlieren) vs. Experimental (OH PLIF overlaid on the schlieren): plots of the evolving ignition kernel at three initial time steps. The first column shows OH density and numerical schlieren on the mid-plane, the second column shows the OH density on the mid-plane and the path-integrated schlieren in the transverse direction, and the third column shows the experimental images on the right that are reproduced from Lefkowitz et al. [6]. Numerical schlieren is defined as the transverse component of the density gradient.

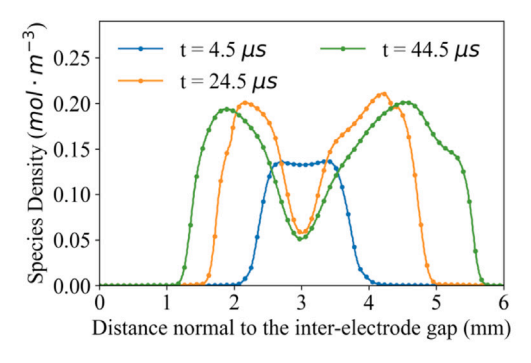
previous discharge pulses. Hence, the computational time to simulate the gap between two pulses varied from $12\ h$ to $36\ h$ using the same computational resources.

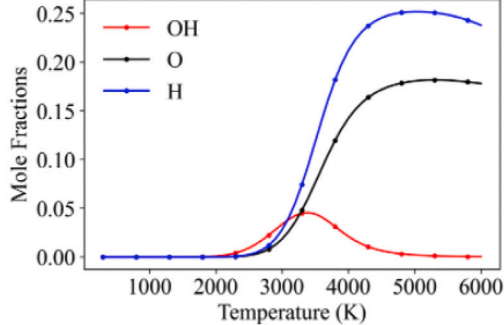
Reynolds-averaged Navier–Stokes (RANS) simulation with the $k\omega$ Shear Stress Transport (SST) model [37] on a coarser mesh (~ 9 million) was used to obtain an initial velocity profile and pressure distribution for the turbulent flow in the subsonic ignition tunnel using the rhoPimpleFoam solver in OpenFOAM. The coarse mesh RANS results were then mapped/interpolated onto a finer mesh to perform LES of the non-reacting flow. Statistically stationary profiles of velocity and pressure from this non-reacting LES were then used as initial conditions for the reacting flow simulations. The velocity profile at the first time step of the reacting flow simulation is shown in Fig. 1(b). As expected, a downstream wake is generated due to the presence of the two electrodes in the flow path. The inter-electrode gap also accelerates the flow velocity to about 13 m/s from the uniform inlet velocity of 10 m/s, although only very locally near the electrodes.

Validation was done by comparing the numerical OH density ($\rho Y_{\rm OH}/W_{\rm OH}$ mol m⁻³) overlaid on the density gradient (i.e., numerical schlieren) with a qualitative OH PLIF overlaid on the schlieren image (as shown in Figs. 2 and 4). The first column shows the OH density and numerical schlieren on the mid-plane, whereas the second column shows the OH density on the mid-plane and the path integrated numerical schlieren in the transverse direction. The path-integrated numerical schlieren along the transverse (x) direction is defined as $(\int_{x_2}^{x_1} (\nabla \rho) \cdot \hat{k} \, dx)$ where x_1 and x_2 are chosen to be the domain integration limits in the transverse direction (–15 mm and 15 mm, respectively). The y-axis is aligned with the mean flow direction and the electrode axes are parallel to the z-axis in these simulations. This path-integrated numerical schlieren shows the connected part of the toroidal kernel, whereas the midplane shows the hole of the toroidal kernel. Ten pulses were deposited

at a frequency of 200 kHz in a premixed methane–air mixture at an equivalence ratio of 0.6, flowing at a mean inlet velocity of 10 m/s. The first pulse deposits 2.5 mJ and all the other pulses deposit 2.9 mJ. These conditions are identical to the experiments in Lefkowitz et al. [6]. The 200 kHz case was chosen, because all the 10 pulses are deposited in 45 μs and hence the overall physical time for which the finest Δt in the inter-pulse gap (0.5–50 ns) is used, is the shortest for this case, which minimizes the computational cost. Also, this case serves as a strict validation target for the model, as interaction of multiple pulses is involved in this case. The compressible flow solver used in this work successfully captures the shock waves generated due to the very high average power deposition (\approx 0.1–1 MW) by each discharge pulse in a small volume of less than 2 mm³. The density gradient (i.e., schlieren), caused by the ignition kernel inception, growth, and convection, is also well captured in the numerical simulation.

Contours of the mass fraction of OH almost completely overlaps with those of temperature, and hence, only the former is shown in Fig. 2(a)-(c) and Fig. 4(a)-(d). Fig. 2(a)-(c) show the comparison of the numerical and experimental results at 4.5 µs (i.e., just before the deposition of the 2nd pulse), 24.5 µs (i.e., just before the deposition of the 6th pulse) and at 44.5 µs (i.e., just before the deposition of the 10th pulse), respectively. The positions of the shock waves due to the previously deposited pulses have been well captured in the simulations. Moreover, the inception of a toroidal kernel (Fig. 2 (b,c)) is also captured well, both by the numerical schlieren and the OH density contours which almost overlap with each other. The slightly larger volume of the downstream lobe of the toroidal kernel (Fig. 2 (b,c)), as compared to the upstream one is due to the convection of the burnt gases along the direction of the background flow, as is also observed in the experiments. The decrease in the OH density in the center of the inter-electrode gap has also been reproduced in the simulations (Fig. 2





- (a) OH density in the inter-electrode gap
- (b) Equilibrium radical mole fractions

Fig. 3. Lowering of OH densities in the inter-electrode gap and a chemical equilibrium analysis at a fixed pressure of 1 atm, and varying gas temperatures.

(b,c)). This is further emphasized by plotting the OH density along a mid-line through the inter-electrode gap in Fig. 3(a).

The reducing minima of OH density with time, in the inter-electrode gap can be attributed to two reasons. The first is the reduced density, due to higher temperatures (in excess of 4000 K) in this region caused by the fast gas heating from the multiple discharge pulses. The second reason can be explained based on the chemical equilibrium mole fractions of OH at different temperatures. Fig. 3(b) clearly shows a peak in the OH mole fraction at a temperature of 3300 K (with a fixed pressure of 1 atm). Whereas, the equilibrium mole fractions of O and H keep rising monotonically with temperature until ~ 5200 K. The marked reduction in OH densities in the inter-electrode gaps, at early time instances (i.e., Fig. 2(a)–(c)) are thus, also due to the relatively higher temperatures (> 3300 K) favoring the formation of O and H over OH.

At longer timescales (165 $\mu s{-}2$ ms), shown in Fig. 4(a)–(d), the toroidal kernel keeps expanding and traveling downstream, with two distinct regions of maximum OH densities that coincide with the numerical schlieren at the mid-plane. The plots in the second column show the path-integrated schlieren which show the connected kernel. These agree better with the experimentally observed path-integrated schlieren images, which also show a connected kernel at longer time instances. The increased luminosity in the OH PLIF signal also indicates the formation of this toroidal kernel, which is well captured in the simulations. At 765 μs and 2 ms (Fig. 4 (c,d)), the OH densities drop to the equilibrium value, and the toroidal kernel keeps expanding to form a continuous flame front indicated by the diminishing gap between the two lobes of the toroid.

3. Results and analysis

This section presents the numerical simulation results of cases at the same equivalence ratio, but with different pulse repetition frequencies (PRF), per pulse energy deposition, and number of pulses. All other modeling parameters and numerical schemes are set same as the validation case discussed in the previous section. Based on the nature of interaction between the ignition kernels generated by different pulses (primarily determined by the pulse repetition frequency, PRF), three regimes were identified in Lefkowitz and Ombrello [4], namely the fully coupled (Section 3.1), partially coupled (Section 3.2), and decoupled regimes (Section 3.3). This interaction can be quantitatively made based on the OH density or temperature increase with every subsequent pulse, leading to varied degrees of high-temperature/radical rich kernel overlap. One of the primary motivations of the current research is to understand the inter-pulse coupling that occurs in each of these regimes, and understand the reasons leading to the reduced ignition probability that was observed at certain intermediate pulse repetition frequencies (2–7 kHz) for relatively leaner mixtures (ϕ < 0.75). Multiple experiments were conducted in Lefkowitz and Ombrello [4], with a

certain degree of stochasticity in the deposition of plasma energy for every pulse, flow turbulence and thermal expansion of each kernel. Thus, at the "same" nominal conditions and settings, some experimental iterations resulted in successful ignition, whereas others did not. Based on the success or failure of ignition, an "ignition probability" was calculated in Lefkowitz and Ombrello [4]. However, such a "stochastic" investigation is not possible with the expensive deterministic CFD simulations. In these simulations, an ignition event is termed "successful" when the ignition kernel defined by the iso-surface of 1300 K, keeps expanding without any assistance of the plasma, beyond 1.5 ms after the last discharge pulse has been deposited. Moreover, based on the simulations performed in this research, 15-20 mm³ was found to be an approximate estimated range of critical volumes of this kernel, beyond which it can expand without additional plasma assistance, for the given mean flow velocity (10 m/s), equivalence ratio (0.69) and inter-electrode gap distance (2 mm). This range of critical volumes also depends on the energy deposited per pulse, number of pulses, and PRF. Furthermore, the volume also depends on the choice of the temperature used to define the enclosing iso-surface. Thus, the estimated range of values provided above correspond to the simulations with the lowest energy per pulse of 5 mJ, with 3 and 5 pulses in the partially coupled regime, both deposited at a frequency of 4 kHz. This case was chosen as the basis to define this criterion, as the volume in the fully coupled case with 3 pulses was bigger than the upper limit of this range (20 mm³), which resulted in ignition success, and that in the decoupled case was smaller than the lower limit of this range (15 mm³) which resulted in ignition failure. Nonetheless, it is difficult to define an exact critical volume and an acceptable time duration at which this volume can be reached, as these heavily depend on the operating conditions and the geometric configuration. Thus, it is worth noting that this volume range and time duration are used consistently to define ignition success or failure for the simulations presented in this section, but these might not necessarily hold for other operating conditions.

Moreover, the equivalence ratio in the simulations was changed from 0.6 (in experiments) to 0.69 with a constant inlet velocity of 10 m/s. This was done because the ignition probability of a single discharge pulse is shown to be \sim 1.0 at $\phi=0.69$, whereas it is only \sim 0.1 at $\phi=0.6$ as per Fig. 5, reproduced from Lefkowitz's and Ombrello's experimental research [4]. Thus, to ensure a higher chance of ignition in expensive deterministic CFD simulations, the equivalence ratio has been increased to 0.69. As per Lefkowitz and Ombrello [4], the minimum ignition power asymptotes to 14.2 W, which corresponds to a minimum total energy of 14.5 mJ in the experiments. To reduce the physical time for which every simulation is run for, (and consequently to reduce the total computational time), the energy per pulse has been set to 5 mJ, and only 3 pulses have been deposited (so that the total energy is 15 mJ, which is very close to the experimental value of 14.5 mJ). While the equivalence ratio and the energy per pulse used in this

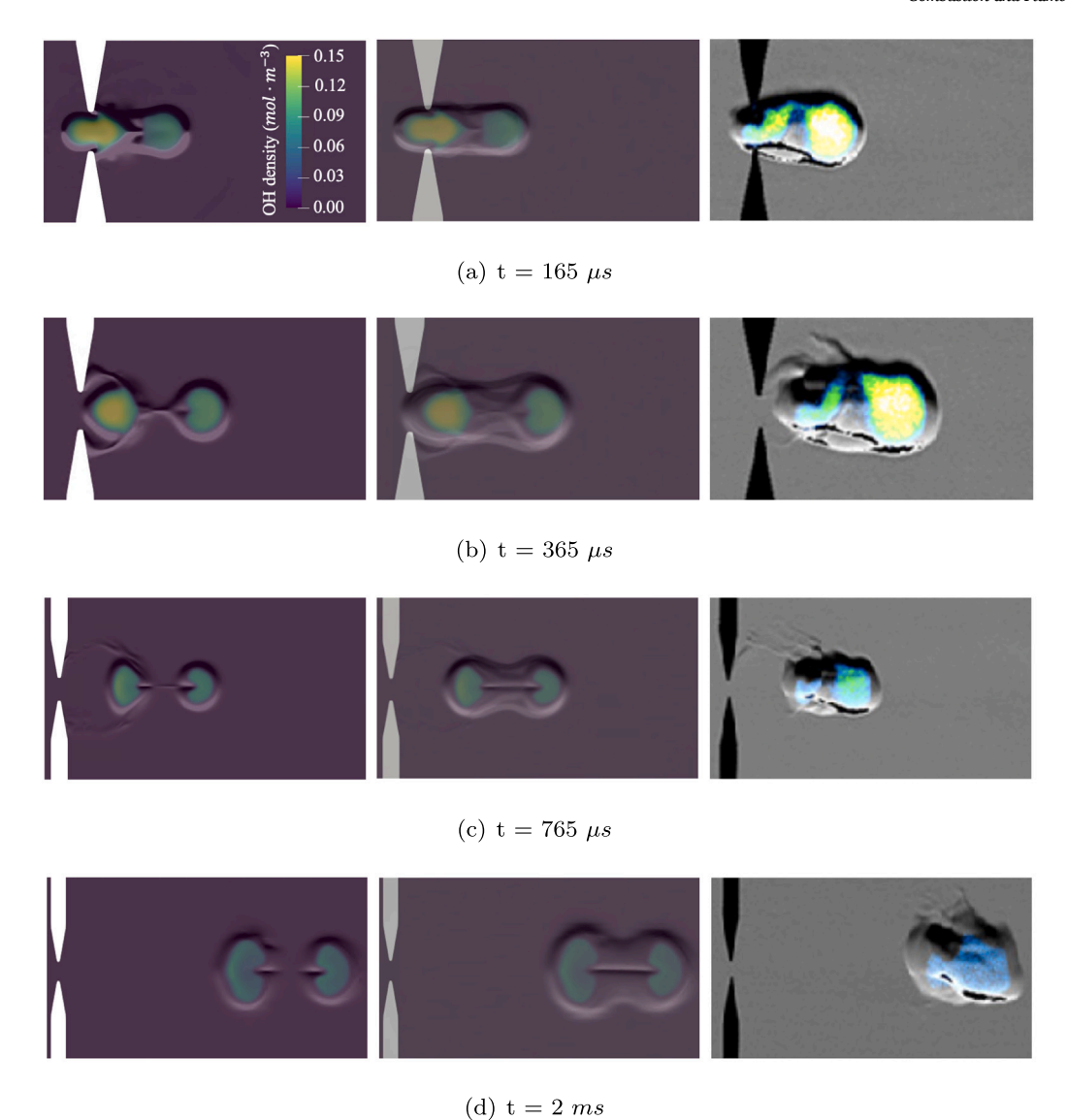


Fig. 4. Computational (OH density overlaid on the numerical schlieren — numerical density gradient) vs Experimental (OH PLIF overlaid on the schlieren): plots of the evolving ignition kernel at four later time steps. Experimental images on the left are reproduced from Lefkowitz et al. [6].

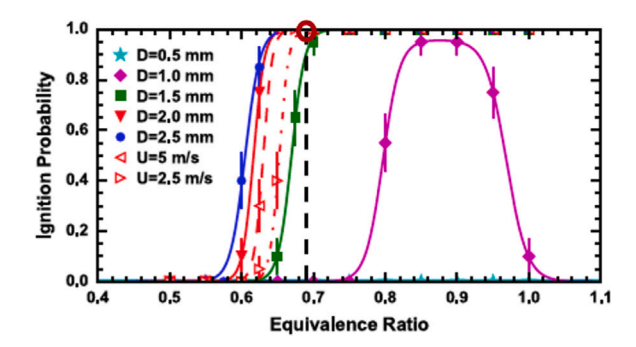


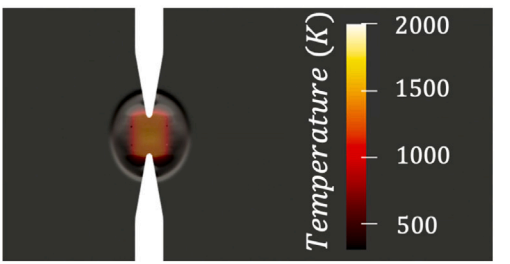
Fig. 5. Ignition probability of a single pulse as a function of the equivalence ratio ϕ (reproduced from Lefkowitz and Ombrello [4]). $\phi=0.69$ is highlighted with a dashed black line.

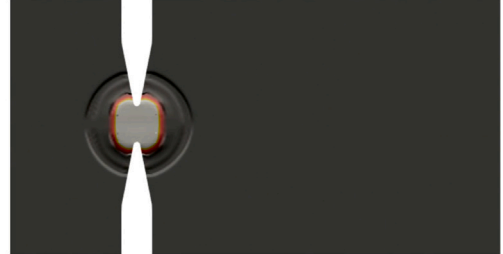
section are different from the ones in the experiments, the same trends were observed as the experiments, albeit with a fewer number of pulses.

The following table 1 summarizes all the simulations and their parameters and outcomes (ignition success or failure).

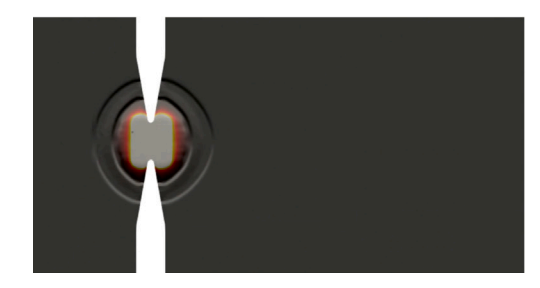
 $\begin{tabular}{ll} \textbf{Table 1} \\ \textbf{Summary of large eddy simulations (LES) presented in Section 3.} \\ \end{tabular}$

Regimes, Parameters, and Ignition Outcome						
Regime	φ	Frequency (kHz)	Energy per pulse (J)	No. of pulses	Sec	Ignition outcome
Fully Coupled	0.69	300	5.0	3	3.1	Successful
Partially Coupled	0.69	4	5.0	3	3.2	Failed
Partially Coupled	0.69	4	5.0	5	3.2	Successful
Partially Coupled	0.9	5	10.0	2	3.2	Successful
Decoupled	0.69	1.5	5	3	3.3	Failed
Decoupled	0.69	1.5	10.0	2	3.3	Successful





(a) Immediately before the 2^{nd} pulse, t = 3.2 μs (b) Immediately after the 2^{nd} pulse, t = 4.0 μs





(c) After the shock from the 2^{nd} pulse emanates (d) Continued growth of the overlapping ignition past the ignition kernel, $t = 6.0 \ \mu s$ kernels after both shocks leave the inter-electrode gap, $t = 8.0 \ \mu s$

Fig. 6. Temperature laid on the numerical schlieren for the fully coupled case (300 kHz) - Ignition kernel growth around the 2nd pulse (i.e., evolution immediately before and after the deposition of the second pulse).

3.1. Fully coupled regime

The case in the fully coupled regime discussed here is characterized with three pulses deposited at an inter-pulse repetition frequency of 300 kHz and a constant per pulse energy deposition of 5 mJ. This case resulted in successful ignition. As is experimentally observed in Lefkowitz et al. [4,6], the fully coupled regime exhibits a 100% ignition probability for three or more pulses. The success of ignition in this case can be simply attributed to the nearly perfect overlap of the high-temperature and radical-rich (OH, O, H, etc.) zones generated by the three pulses that synergistically helps in igniting the mixture. The radical-rich zones and high-temperature zones almost completely overlap with each other, and hence only the latter are shown in the figures which follow. Moreover, due to the high rate of energy deposition in every nanosecond discharge pulse, each pulse produces a shock wave that emanates radially outwards which eventually turns into a compression acoustic wave. The total time taken for production and propagation of this shock wave and its conversion into a compression acoustic wave ($\sim 5-10 \mu s$) is comparable to the inter-pulse time (3.33 µs, frequency - 300 kHz). Consequently, the shock-wave produced by the next discharge pulse emanates outside the region of the inter-electrode gap, and thus does not affect the next discharge pulse and the interaction of the overlapping kernels produced by the two overlapping discharge pulses. In these microsecond level timescales, the translational bulk motion of the ignition kernel is almost negligible at the given flow velocity of 10 m/s (i.e., only 33.3 microns). Thus, the almost complete overlap of high-temperature and radical-rich ignition kernels results in increased ignition probability.

Fig. 6 shows contours of temperature overlaid on the numerical schlieren (*i.e.*, density gradient). The growing single unified kernel after the deposition of the subsequent pulses emphasizes the observation of overlapping kernels. After the three discharge pulses, the ignition kernel grows further, and convects due to the background mean flow. The ignition kernel transforms to a primary toroidal shape and two smaller lobes are also observed to grow along the electrodes, in the transverse direction (Fig. 7(d)–(f)).

Fig. 7(a)–(f) show the evolution of the ignition kernel. Projections of iso-surfaces of 1300 K on the center-plane are chosen to depict the ignition kernel, which are colored with the heat release rate in this figure. The qualitative features and quantitative trends discussed in this and the following sections remain agnostic of the choice of the iso-surface beyond a minimum temperature of 1200 K. These are overlaid on the numerical schlieren to highlight flow features, such as emanating shock waves and ignition kernel evolution. The heat release rate decreases and eventually reduces to almost zero after the formation of burnt gas products. After expanding beyond a minimum ignition volume, the kernel converts into a self sustained ignition front and grows despite the heat and radical diffusion losses and shearing caused by the flow, and eventually results in successful flame propagation.

3.2. Partially coupled regime

The partially coupled regime is mainly characterized in the pulse repetition frequency range of 2-7 kHz, as per Fig. 6 of Lefkowitz et al. [4]. This regime has a very "diffused" interaction of hot spots produced by subsequent discharge pulse, which interfere destructively or constructively [4] with each other. Simulations in this study were conducted with the same energy per pulse and equivalence ratio as the fully coupled case (i.e., 5 mJ per pulse and 0.69, respectively), but at a PRF of 4 kHz, which corresponds to an inter-pulse time period of 2.5×10^{-4} s. In this time period, the ignition kernel produced by the previous discharge pulse only travels approximately 2.5 mm downstream, at a bulk flow velocity of 10 m/s. In contrast, the shockturned acoustic wave generated by the subsequent discharge pulse, travels at an average Mach number of 1.1 in the first 4 μs and hence convects across a radius of approximately 2.5 mm, given that it travels in the mixture with an average temperature of 650-750 K. Thus, the shock wave produced by the subsequent discharge pulse can easily catch up and interact with the ignition kernel produced by the previous discharge pulse due to their similar convection timescales. The contour plots of temperature overlaid on the numerical schlieren in Fig. 8

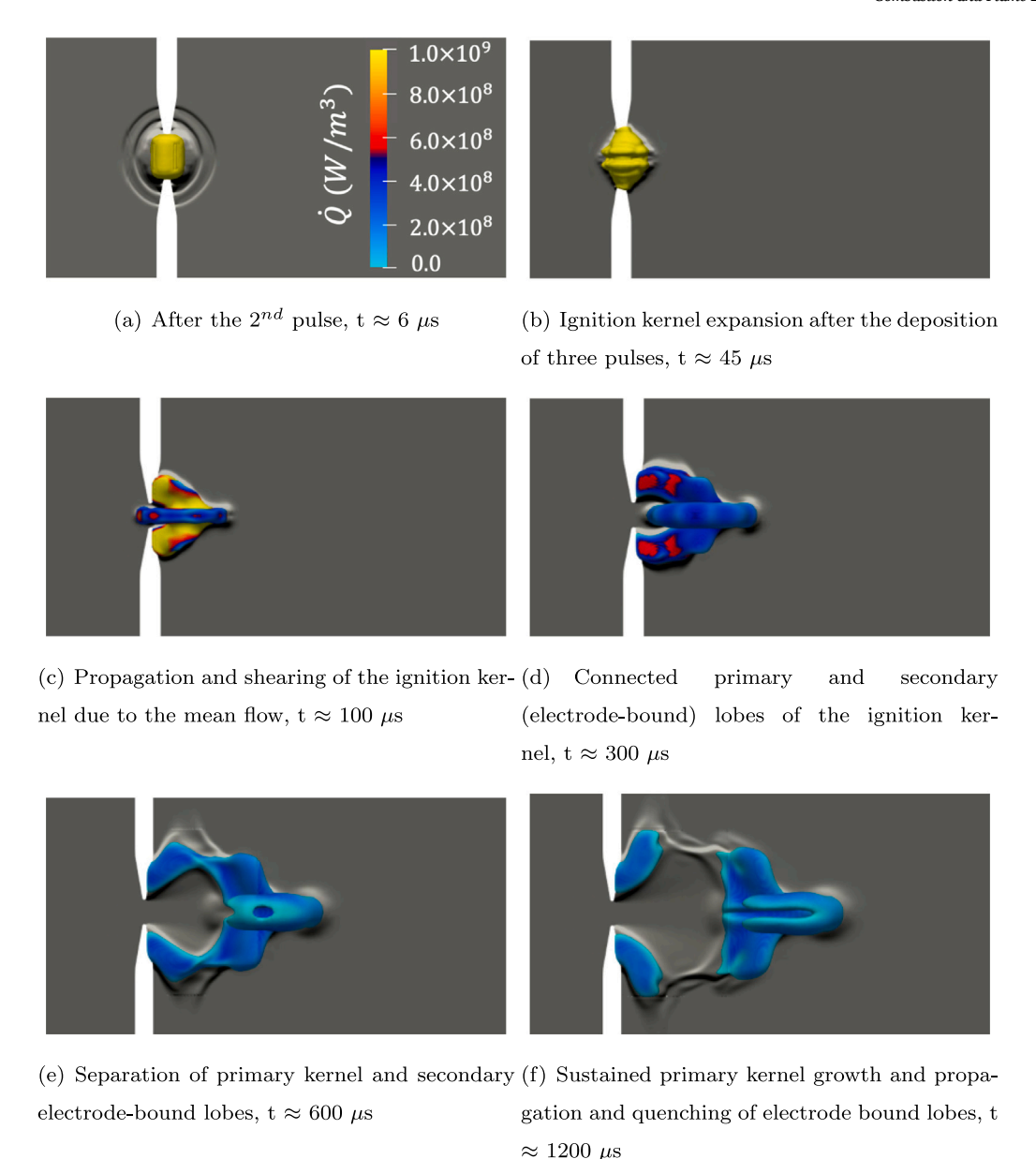
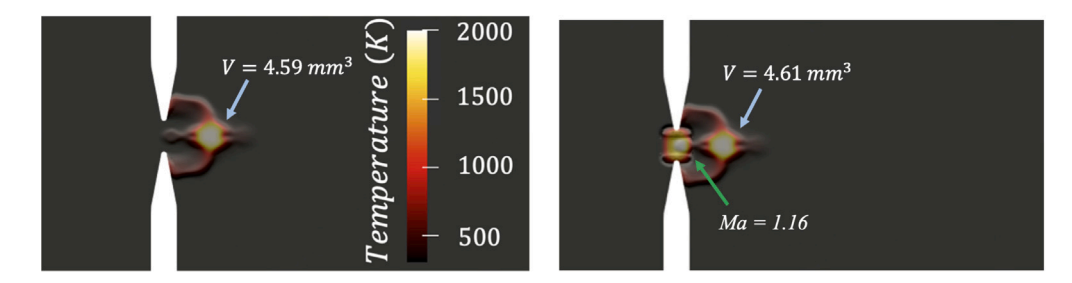


Fig. 7. Projection of the iso-surface of 1300 K (to represent ignition kernel) on the center-plane, colored by the heat release rate overlaid on the numerical schlieren (i.e., density gradient) for the fully coupled case (300 kHz), showing successful ignition. Increasing kernel volume and reducing heat release rate show ignition kernel expansion along with conversion of reactants to products.

show this interaction, which appears to be destructive. Specifically, as the shock wave passes over the ignition kernel produced by the previous discharge pulse, the convective heat loss increases locally. This is shown by quantifying the magnitude of the convection term of the energy equation (i.e., $\rho C_p u_i \partial T/\partial x_i$) in Fig. 9(a)–(d). As can be seen in this figure, the convective loss starts increasing at the trailing edge (upstream edge) of the kernel produced by the first (previous) pulse, when the shock wave comes in contact with the trailing edge. It then increases at the leading edge (i.e., the downstream edge) of the kernel, and eventually reduces as the shock gets converted to an acoustic wave, and emanates radially outward, past the kernel produced by the first pulse.

This effect can be seen as the reduction in the volume of the kernel (from each discharge pulse) when the shock-turned acoustic wave from the subsequent discharge pulse reaches the preceding kernel in Fig. 8(f). This ignition kernel volume is defined as the volume enclosed by the iso-surface of temperature of 1300~K.

Fig. 10 shows the evolution of the volumes of the ignition kernels produced by the first and second pulses, for 200 and 350 μs after the second and third discharge pulses are deposited, respectively. It also shows the evolution of the final kernel after the third (last) pulse is deposited. To maintain consistency in the plot, the start time of the third kernel is from 250 µs after the third discharge pulse was deposited. The time is plotted in log-scale to capture the volume of the kernels at the first 10 µs after the subsequent discharge pulses and that at longer time instances of 75 and 200 μs (for first kernel) / 100 and 350 μs (for second kernel) after the subsequent discharge pulse. This way of plotting is chosen to highlight the different constructive and destructive effects governing the evolution of the ignition kernels. A sudden reduction of about 19% in the volume of the first kernel and that of about 16% in the volume of the second kernel between 4-8 µs after the deposition of the subsequent pulse, clearly shows how the shock-turned acoustic waves produced by the second and third discharge pulses, respectively, negatively affect the evolution of the preceding ignition kernel. This destructive interaction effect of reduction in volume can



(a) Immediately before the 2^{nd} pulse, $t=245~\mu s$ (b) Immediately after the 2^{nd} pulse, $t=251~\mu s$



(c) Before the shock from 2^{nd} pulse reaches the (d) When the shock reaches the trailing edge of kernel produced by the 1^{st} pulse, $t = 252 \ \mu s$ the kernel produced by the 1^{st} pulse, $t = 254 \ \mu s$



(e) When the shock reaches the leading edge of (f) After the shock-turned-acoustic wave emthe kernel produced by the 1^{st} pulse, $t = 255 \mu s$ anates past the kernel produced by the 1^{st} pulse,

$$t = 257 \ \mu s$$

Fig. 8. Temperature overlaid on the numerical schlieren for the partially coupled case (4 kHz) - Ignition kernel growth around the 2nd pulse. The max Mach numbers of the shock-turned-acoustic wave have also been listed.

also be visually deduced by comparing the sizes of the downstream kernels in Fig. 8(a) and (e), (f). Following this, the kernels keep growing gradually for the next \sim 65 (first kernel) / 90 (second kernel) μs by about 8%-10%. This gradual increase in volume is attributed to the heat release rate of the expanding kernel. This rise is then followed by a steady decrease in the volume of the kernels at longer timescales. This has been attributed to the diffusion loss of both temperature and radicals, which happens when the kernel does not grow past a minimum threshold size (i.e., critical volume) for it to keep expanding as an ignition front. Thus, the initial rapid decrease in volume due to the kernel-shock(-turned acoustic wave) interaction precludes it from reaching a large enough volume with a high enough concentration of radicals and temperature. This destructive interaction coupled with the diffusion losses ultimately results in failed ignition for this case. It can also be seen from Fig. 10 that the volume of the second kernel immediately after the third pulse is deposited, is around 8.4 mm³, whereas that of the first kernel immediately after the second pulse is deposited is 4.6 mm³, which suggests that the kernel volume does increase by about 82% with addition of the new pulse — an important constructive interaction effect. Similarly, the final kernel volume after 250 μs after the third pulse is deposited is $\sim 12.5 \text{ mm}^3$, which is $\sim 49\%$

larger than the second kernel immediately after the third pulse was deposited. This is primarily due to the partial, though non-negligible, overlap of the new kernel with the previous kernel, which assists the increased growth of the new kernel due its growth in a region of relatively higher temperature and higher radical concentration. This partial overlap can be seen from Fig. 8(f). Depositing three pulses at 0, 250, and 500 µs, does result in the formation of an overlapping kernel at longer time-scales, as can be seen in Fig. 11(a). But the extent of overlap (constructive effect) is not sufficient to cause the growth of the kernel volume to a big enough value for it to outweigh the diffusion losses that occur at longer timescales, which eventually result in diminishing kernel volume in Fig. 11(c). Unlike the fully coupled case, the heat release rate reduction happens with a reduction in the kernel volume (Fig. 11), which shows that both radical and heat diffusion losses preclude formation of burnt gas products. The eventual reduction in the final kernel volume has also been plotted in Fig. 10, which shows that the kernel grows to a volume of $\sim 14.5 \text{ mm}^3 \text{ till } 950 \,\mu\text{s}$ (shown by the third point on the blue curve), but then shrinks due to diffusion losses at longer timescales. The negative contribution of the shock-turnedacoustic wave can also be seen by comparing Fig. 10 with Fig. 16, where the latter shows that the kernel defined by the 1300 K iso-surface

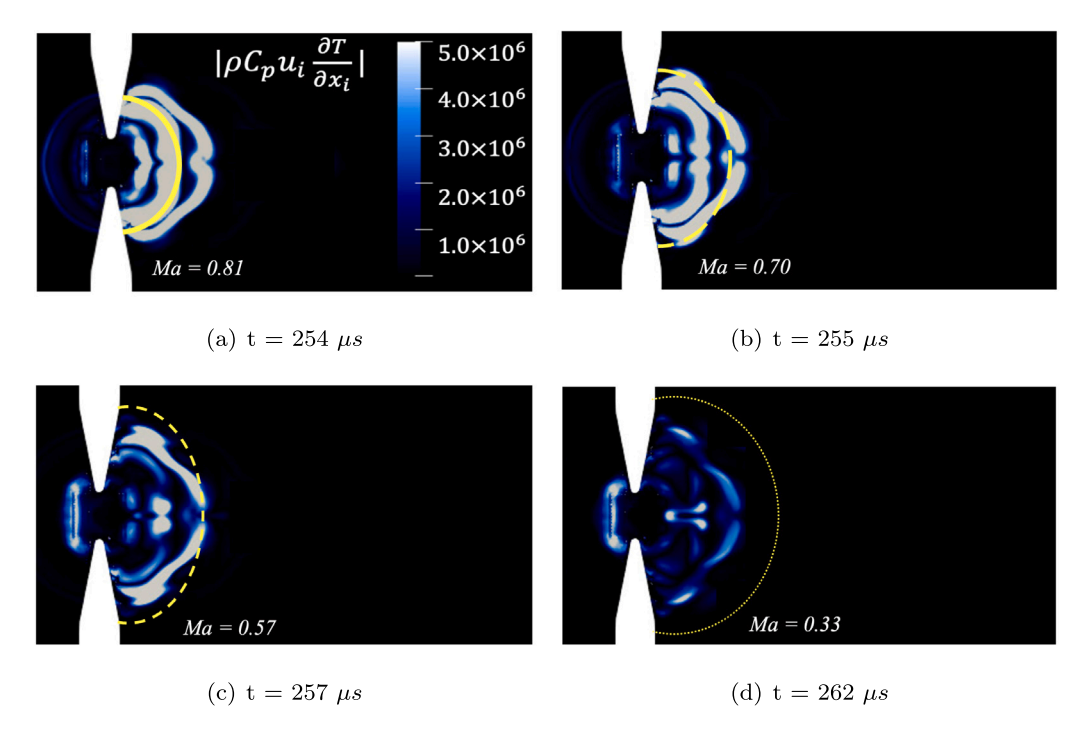


Fig. 9. Partially coupled case (4 kHz) - Convection heat loss around the 2nd pulse. The yellow spline represents the position of the shock-turned-acoustic wave, with the diminishing thickness of the line representing its diminishing strength (Mach number). Absolute values of the negative convection term (convection loss) have been shown.

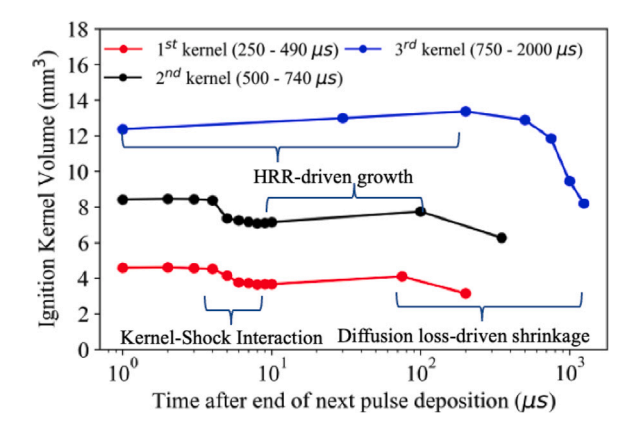


Fig. 10. Evolution of the volume of the preceding ignition kernel after the deposition of the subsequent pulse. The legend shows the time window considered for plotting the volumes of each kernel. This volume is defined as the volume enclosed by the iso-surface of 1300 K.

sustains for a much longer time (i.e., till 750 μs instead of 450 μs). Also, the volume of the first kernel at the same time instances in the decoupled case are bigger than those in the partially coupled case, since the latter has an additional destructive interaction due to the shock-turned-acoustic wave, whereas the former does not. These details are also explained in Section 3.3.

Consequently, when a sufficient number of pulses are deposited, successful ignition in this regime may be observed due to the dominance of the constructive interaction over the destructive interaction. This was evaluated by adding two more pulses to the previous case with three pulses. Successful ignition was observed based on the expanding ignition kernel volume at longer timescales of up to 3.2 ms, as shown in Fig. 12. Interestingly, at longer timescales (beyond 1.5 ms), the projected area of this expanding kernel on the mid-plane kept decreasing with time (see the cross sections marked by red color in Fig. 13). But the kernel volume actually kept expanding in the transverse direction, in a dual tear-drop shape which is constricted in

the center, driven by the counter-rotating vortex pair (CVP) behind the kernel. This is unlike the previous cases, where the kernel growth was predominantly in the longitudinal direction. This evolution of the final kernel after the deposition of five pulses has been plotted using the iso-surfaces of 1300 K in Fig. 13. The addition of two extra pulses increased the partial coupling of the kernels, which eventually helped form a self-sustaining ignition kernel. Thus, the competition between these constructive (assistance provided by the preceding kernel to allow expansion of the next kernel in a high-temperature and radical-rich region) and destructive (shock-turned-acoustic wave driven kernel volume reduction at shorter timescales after next pulse deposition and diffusion losses at longer timescales) effects could help explain the increase in ignition probability with increasing number of pulses in the partially coupled regime, which was found in the experiments [4].

Moreover, when conditions are made more favorable such that a single pulse can raise the temperature by about 1500-1800 K, successful ignition and flame formation can be achieved in the partially coupled regime with fewer pulses. This is shown in Fig. 14, where the equivalence ratio is 0.9, the pulse energy is 10 mJ, and the PRF is 5 kHz. In this case, the kernel produced by the first pulse has a high enough temperature (average temperature of ~ 1700 K) and suitable concentration of radicals for it to ignite completely and form a selfsustaining flame front. The background flow shearing and diffusion losses do cause it to stretch and quench locally, but is has been shown in Taneja et al. [24], that this single pulse can eventually form a flame front. Nonetheless, it takes more than 2 ms for this kernel to become a sustained flame front, which can continue to expand. When another pulse with the same energy is deposited, the subsequent kernel expands in a region with higher average temperature (~ 1000-1200 K) and rich with radicals such as OH, O and H, created by the first pulse. The kernel produced by the first pulse travels about 3 mm downstream in the same time duration. This assistance (provided by the kernel from the first pulse) for the next kernel (produced by the second pulse) results in a synergistic effect, where a small portion of the kernel, which travels downstream, locally ignites, expands as a toroidal lobe and eventually connects with the previous kernel (which has traveled further downstream in the mean time). This sequence of events can be seen in Fig. 14 ((e)-(g)). This "bridges the gap" between the ignition

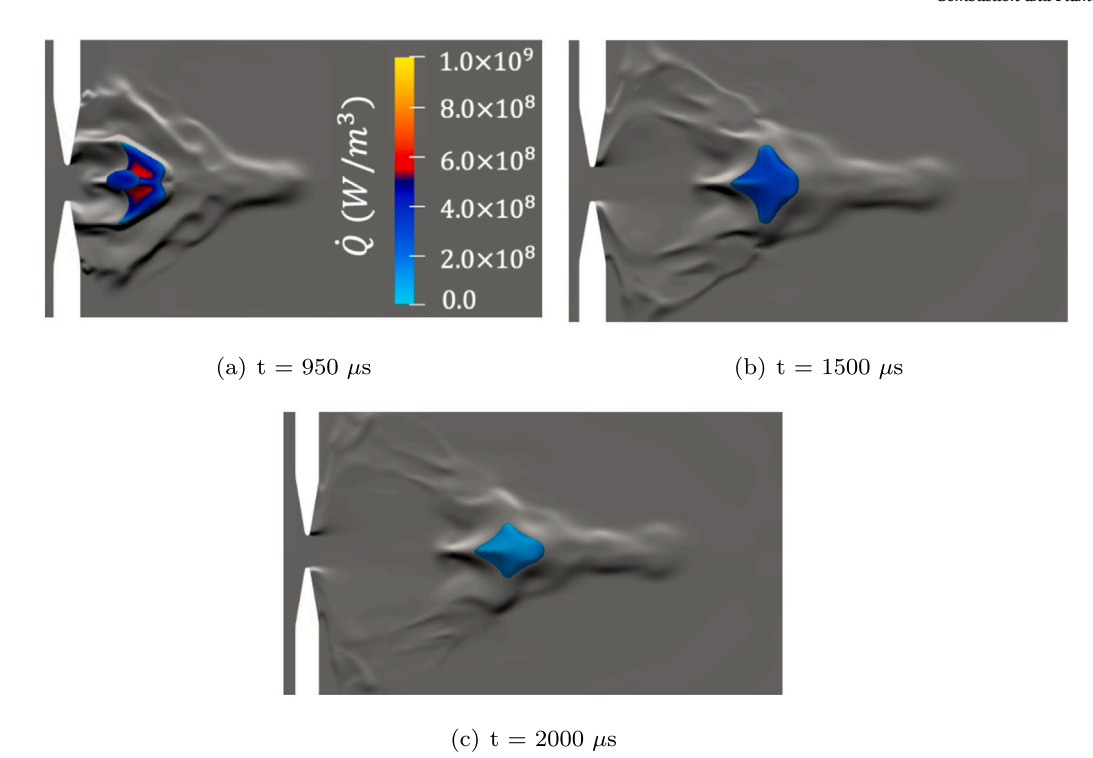
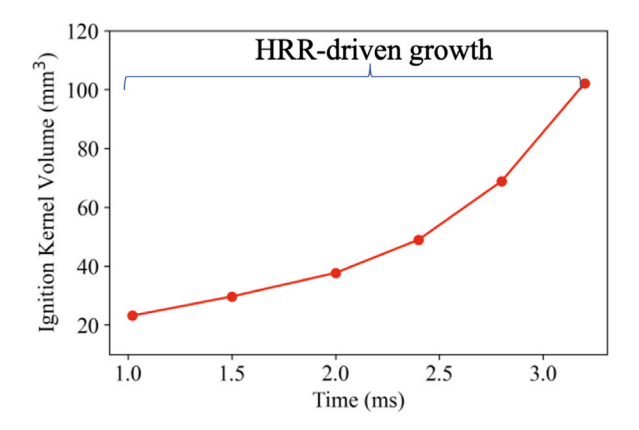


Fig. 11. Projection of the iso-surface of 1300 K (to represent ignition kernel) on the center-plane, colored by the heat release rate overlaid on the numerical schlieren (i.e., density gradient) for the partially coupled case with three pulses, showing evolution at wider timescales. Decreasing kernel volume and heat release rate are indicative of ignition failure.



 $\textbf{Fig. 12.} \ \ \textbf{Increasing kernel volume after deposition of five discharge pulses}.$

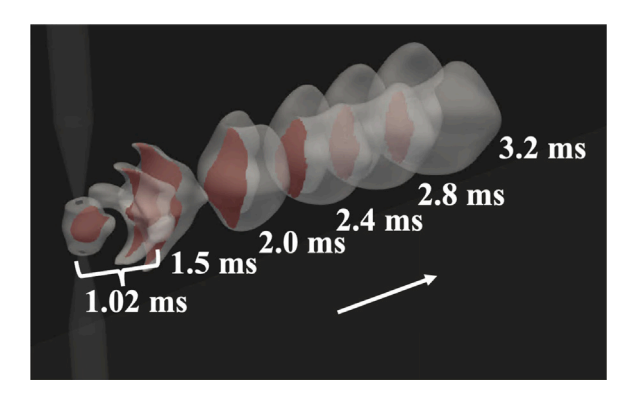


Fig. 13. Time history of the developing ignition kernel represented as iso-surfaces of temperature of 1300 K after depositing 5 discharge pulses. The projection of this kernel on the domain center-plane is also shown in red.

kernels produced by the two consecutive discharge pulses and forms a much larger and connected flame front. Thus, altering the operating conditions can result in successful ignition even in the partially coupled regime, which has also been experimentally observed in [4]. Physically, this depends on whether the constructive or the destructive effects, discussed earlier, dominate.

3.3. Decoupled regime

When the pulse repetition frequency (PRF) is lower than ~2 kHz, the ignition kernels produced by different pulses do not interact with each other. This is because each high-temperature and radical-rich kernel travels downstream by 0.4-1 cm between two subsequent discharge pulses at a background velocity of 10 m/s, depending on the exact pulse repetition frequency (PRF). The approximate radius of the ignition kernel after a few hundreds of microseconds post deposition of the discharge pulse (energy per pulse of 5 mJ) is about 2-5 mm based on the applied voltage, pulse duration, and the inter-electrode gap. Thus, every discharge pulse is deposited in almost the same fresh gas-like thermochemical conditions, when the inter-pulse time is ~ 0.5 – 1 ms. Hence, there is typically no synergy between ignition kernels produced by subsequent discharge pulses. This regime is referred to as the decoupled regime. These findings are depicted in Fig. 15, which show the contours of temperature overlaid on the numerical schlieren for a case with an equivalence ratio of 0.69 and a pulse repetition frequency (PRF) of 1.5 kHz. Four instances - t = 245 µs after the first pulse, $t = 700 \mu s$ which is $\sim 35 \mu s$ after the second pulse, t =1.36 ms which is 26 μ s after the third pulses, and t = 1.60 ms which is $\sim 270~\mu s$ after the third pulse — are shown in Fig. 15. Unlike the fully coupled and partially coupled cases, no constructive interaction between the kernels is observed. Moreover, diffusion losses preclude the temperature, radical densities, and kernel volume from increasing beyond certain thresholds which can cause the kernel to keep expanding as a self-sustained ignition front. The 10 m/s background flow also causes shearing and quenching of the ignition kernel, as is seen from the reduced temperatures and the numerical schlieren plots. Each kernel

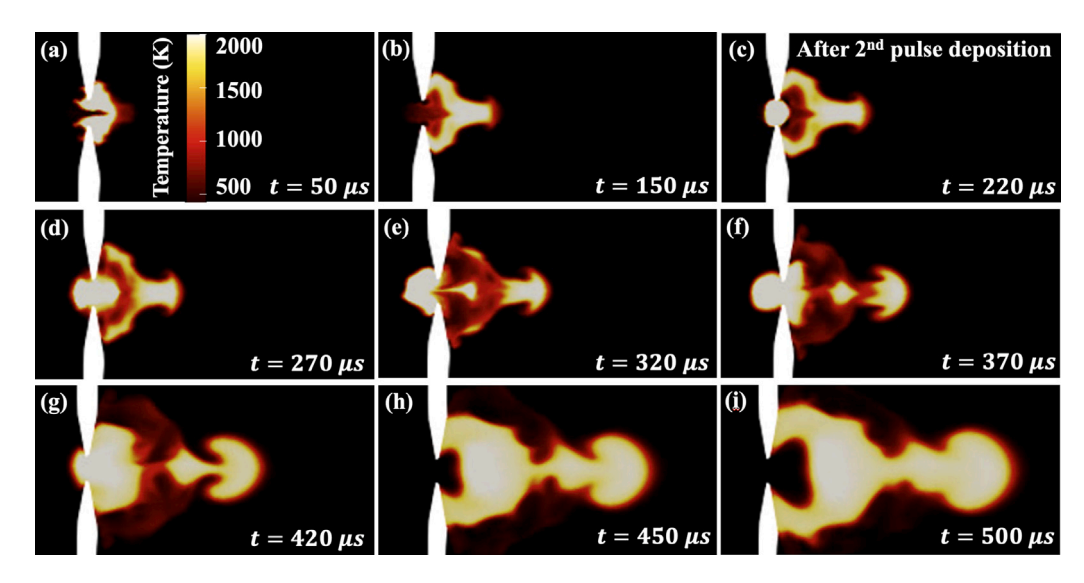
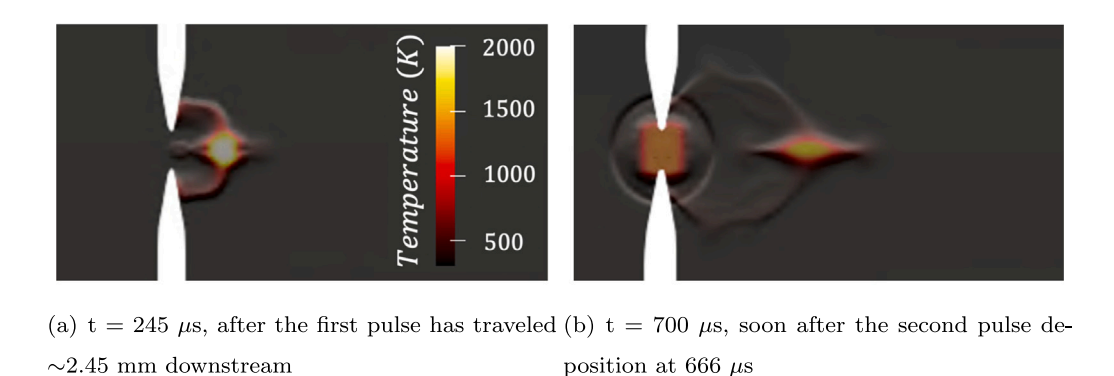
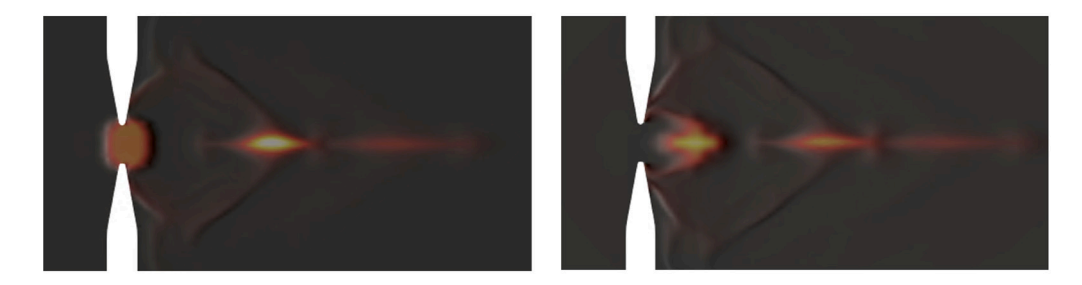


Fig. 14. Rapid flame formation due to the constructive interaction of two consecutive ignition kernels formed in the partially coupled regime. $\phi = 0.9$, Frequency = 5 kHz, Energy per pulse = 10 mJ.





(c) t = 1360 μ s, 26 μ s after depositing the third (d) t = 1600 μ s, 270 μ s after depositing the third pulse pulse, all kernels quench

Fig. 15. Temperature overlaid on the numerical schlieren for the decoupled case (1.5 kHz), resulting in failed ignition.

which starts as a cylinder expands radially, and contracts axially as it propagates downstream. Consequently, the surface area to volume ratio keeps increasing, which enhances heat and radical loss to the mean flow thereby resulting in ignition failure.

Fig. 16 shows the kernel volume evolution of the first two kernels in the decoupled regime. Since this case was initialized from 250 μ s (i.e., from data just before the second pulse deposition in the partially coupled case in Section 3.2), the time 0 on the *x*-axis of Fig. 16

corresponds to 250 μs after each pulse is deposited. As is seen from this figure, the chemical heat release rate (HRR) causes growth of the kernel until about 375 μs after the pulse is deposited, but it eventually decreases due to diffusion losses. It is worth noting, that the volume of the first kernel in this case, at around 400 μs is more than 4.2 mm³, which is almost 32% larger than the volume of the first kernel in the partially coupled case around the same time (see Fig. 10). This further shows that since the shock-turned-acoustic wave does not destructively

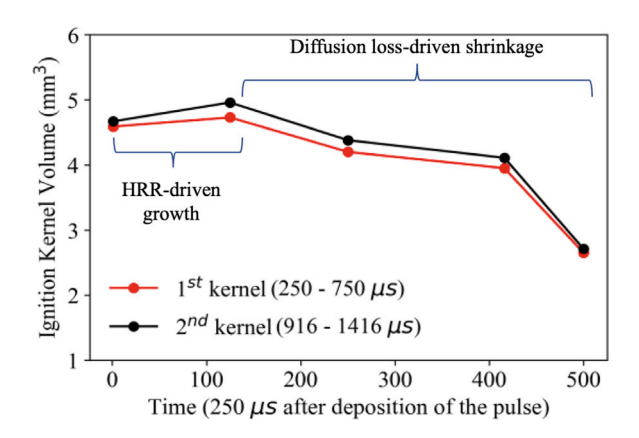


Fig. 16. Evolution of the first and second kernel volumes in the decoupled regime This volume is defined as the volume enclosed by the iso-surface of 1300 K.

interact with the preceding kernel in the decoupled case, the final volume is larger in the decoupled case, as compared to that in the partially coupled case. As a result, the high temperature (1300 K) kernel also sustains for a longer time in the decoupled case before quenching due to diffusion losses, as compared to the partially coupled case. However, since there is also no constructive coupling in this regime, the volume of the second kernel remains almost the same as that of the first kernel. This is markedly different from the partially coupled case, where the volume of the second kernel is almost 82% larger than the first kernel.

However, in the experiments of Lefkowitz and Ombrello [4], the ignition probability in this regime is found to increase linearly with the number of pulses. It is hypothesized that this is not because of any cumulative benefits of multiple pulses in the decoupled regime, but is probably because of the stochastic nature of the experiment in this regime, where only a very few number of pulses with a higher energy can ignite the mixture, thereby resulting in a higher ignition probability. This behavior is not possible to reproduce in the fully deterministic CFD simulations, unless the energy is increased artificially to cause ignition. This is done by increasing the energy of only two pulses to 10 mJ, as was also done in the partially coupled case. Figs. 17 and 18 show how two pulses with a high enough energy deposition (10 mJ instead of 5 mJ) can lead to ignition, because the ignition kernel created by the second pulse, which is now bigger in volume due to the higher energy deposition, does expand partially in a radical-rich and high-temperature zone created by the first pulse. It is worth noting that the shock-turned acoustic wave created by the second pulse does not significantly impact the kernel produced by the first pulse (as seen in Fig. 18(a)-(d)), unlike the partially coupled regime. This is simply because the first kernel travels a further distance due to the longer inter-pulse time in the decoupled regime, such that the shock wave loses its energy and becomes a weak acoustic wave by the time it interacts with the first kernel. At such high pulse energies, the range of frequencies spanning the definition of "decoupled regime" should therefore be changed, because the pulses shown in Fig. 18, clearly do have constructive interaction. The leading edge of the second kernel spreads and connects with the trailing edge of the previous kernel, thereby bridging the gap between the two kernels. Although the leading edge of this bigger second kernel also quenches locally, the trailing edge further expands. This expansion of the trailing edge continues beyond 3 ms, and thus, the case can be considered a successful ignition kernel.

4. Conclusion

Large eddy simulations (LES) were performed to understand the effect of the pulse repetition frequency (PRF), number of pulses, and energy per pulse, on the success of ignition of a lean methane-air

premixed mixture flowing at a velocity of 10 m/s, using pin-pin electrodes separated by 2 mm. These simulations were motivated primarily by the experimental findings of Lefkowitz et al. [4–6]. A phenomenological plasma model [21] coupled with a compressible reacting flow solver [27] was used for all the simulations.

Numerical schlieren (i.e., density gradient) and OH density were compared with the experimental schlieren and OH PLIF for a 200 kHz PRF case with 10 pulses [6] to validate the modeling strategy. The lower mole fractions of OH in the inter-electrode gap during the deposition of the pulses was attributed to the formation of O and H over OH at high temperatures (> 3300 K) produced by the discharge pulses. Moreover, the overall gas density (and thus, OH density) also reduces in the inter-electrode gap due to the same reason. After the discharge pulses were turned off, the concentration of OH aligned with the toroidal ignition kernel. These observations are consistent with the experimental trends. Moreover, the position of the shock waves were also well captured by the solver and agree well with the experimental schlieren.

Based on the interaction between ignition kernels produced by subsequent pulses in a pulse train, three regimes were defined in Lefkowitz and Ombrello [4] - the fully coupled regime, the partially coupled regime, and the decoupled regime. These regimes depend on various factors, including the PRF. For the operating parameters (i.e., flow velocity of 10 m/s, energy per pulse of 2.5–5 mJ, equivalence ratio ϕ of 0.6-0.69, inter-electrode gap distance of 2 mm) used in this work, the fully coupled regime exists for all PRF greater than 7 kHz, the partially coupled regime spans PRFs between 2 and 7 kHz, and the decoupled regime exists for PRF lesser than 2 kHz. It was also shown that changing the energy per pulse to 10 mJ from 5 mJ, resulted in constructive partial coupling of kernels produced by consecutive ignition kernels even with a PRF of 1.5 kHz (that falls in the decoupled regime for lower energy per pulse), thereby bridging the gap between the two kernels. This shows that the boundaries of these regimes depend on the combination of the operating parameters. The complete overlap of ignition kernels produced by the discharge pulses at high frequencies (such as 200 kHz and 300 kHz shown in this work) results in successful ignition and flame formation in the fully coupled regime. On the other hand, the total lack of synergy between ignition kernels produced by consecutive pulses at lower frequencies resulted in ignition failure in the decoupled regime. Interesting constructive and destructive effects at intermediate frequencies were observed in the partially coupled regime. At a PRF of 4 kHz, the shock-turnedacoustic wave produced by the next pulse was shown to increase the convective heat loss when it passed over the kernel produced by the previous discharge pulse, thereby resulting in an almost-instantaneous reduction of the kernel volume by 16%-19%. Following this, the kernel volume first increases due to chemical heat release and then decreases due to diffusion losses at longer time-scales. The dominance of the destructive effects over the constructive effect inhibits the formation of a self-sustaining ignition kernel with three pulses in the partially coupled regime. Successful ignition was also shown in the same regime, by depositing two additional pulses. The time-history of the kernel volume showed that it expands in the transverse direction at longer time-scales. When the kernel produced by the next pulse is assisted by the high temperature and radical concentration created by the previous pulse, due to partial overlap, it helps in bridging the gap and forming a self-sustained ignition front. The dominance of one effect over the other was shown by comparing cases in the partially coupled regime with different energies per pulse (5 mJ vs. 10 mJ), different equivalence ratios (0.69 vs. 0.9), with slightly different PRFs (4 kHz vs. 5 kHz) and by increasing the number of pulses.

CRediT authorship contribution statement

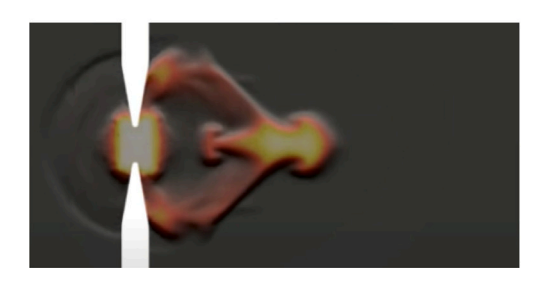
Taaresh Sanjeev Taneja: Writing – original draft, Visualization, Validation, Software, Methodology, Investigation, Formal analysis, Data

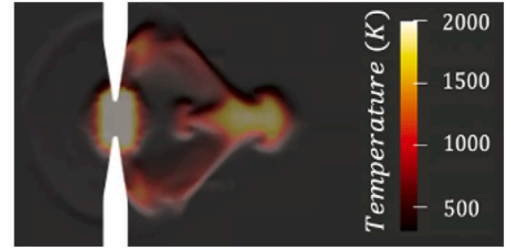




(a) $t = 668 \mu s$, immediately after the second (b) $t = 672 \mu s$, shock gets converted to an accuspulse is deposited, shock propagation starts

tic wave which reaches the trailing edge of the kernel produced by the previous pulse

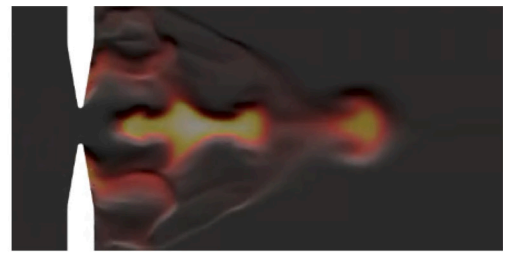




(c) t = 674 \(\mu\)s, shock-turned-acoustic wave loses (d) Almost no change in the previous kernel volstrength without significantly impacting the ker- ume, t = 678 μs nel produced by the previous pulse

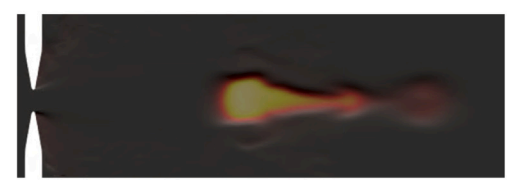
Fig. 17. Temperature overlaid on the numerical schlieren for the decoupled case (1.5 kHz), showing negligible interaction of the shock and the downstream ignition kernel.





(a) t = 1 ms, trailing edge of the first kernel and (b) t = 1.25 ms, leading edge of the first kernel leading edge of the second kernel connect starts to quench, second kernel grows further





(c) t = 2.2 ms, trailing edge of the second kernel (d) t = 3 ms, formation of sustained ignition kergrows further

Fig. 18. Temperature overlaid on the numerical schlieren for the decoupled case (1.5 kHz) with 2 pulses with energy of 10 mJ per pulse, resulting in successful ignition, ϕ = 0.69.

curation, Conceptualization. **Timothy Ombrello:** Writing – review & editing, Investigation, Conceptualization. **Joseph Lefkowitz:** Writing – review & editing, Investigation, Conceptualization. **Suo Yang:** Writing – review & editing, Validation, Supervision, Resources, Project administration, Methodology, Investigation, Funding acquisition, Formal analysis, Conceptualization.

Declaration of competing interest

The authors declare that they have no known competing financial interests or personal relationships that could have appeared to influence the work reported in this paper.

Acknowledgments

S. Yang acknowledges the grant support from NSF CBET 2002635. T.S. Taneja acknowledges the Doctoral Dissertation Fellowship (DDF) and the UMII MnDRIVE Graduate Assistantship from the University of Minnesota. The authors also acknowledge the Minnesota Supercomputing Institute (MSI) and Prof. Graham V. Candler for the computational resources.

Appendix. Details of the pressure-based compressible flow solver

The solver developed in this work was adapted from the *reactingFoam* solver in OpenFOAM-6 [28], which was coupled with Cantera [38] in-house [27,39]. This solver works suitably for both low-Mach subsonic flows and transonic flows without compromising on the computational efficiency. The transient pressure correction equation is modified by introducing the compressibility, $\psi = \rho/p$, and converting the traditionally solved pressure Poisson equation, which is elliptic, to a hyperbolic equation, as is explained in Moukalled and Darwish [40].

The semi-discretized form of the pressure correction equation used in this solver is given in Eq. (A.1):

$$\frac{\partial (\psi^n p^{n+1})}{\partial t} + \nabla \cdot (\psi^n (\underline{A}^{-1}(u)\underline{H}(u))^* p^{n+1}) - \nabla \cdot (\rho^n (\underline{A}^{-1}(u))^* \nabla p^{n+1}) = 0 \tag{A.1}$$

In Eq. (A.1), the variables with * are at the predicted state obtained after solving the momentum equation, the variables with n are computed at the previous time step and the ones with $^{n+1}$ are to be computed at current time step. Matrices A(u) and H(u) are defined from the matrix of coefficients, M(u), in the semi-discretized form of the momentum equation (*i.e.*, Eq. (1)), which can be written as follows,

$$M(u)\overline{u} = -\nabla p \tag{A.2}$$

$$\underline{A}(u) = diag(\underline{M}(u)) \tag{A.3}$$

$$H = A(u)\overline{u} - M(u)\overline{u} \tag{A.4}$$

The convective term $(\nabla \cdot (\psi^n(\underline{A}^{-1}(u)\underline{H}(u))^*p^{n+1}))$ renders Eq. (A.1) its hyperbolic nature at high Mach numbers. For steady state flows, Eq. (A.1) can be obtained from the steady-state version of the compressible continuity equation, which has two contributions to the total mass flux correction (m_f') across a face. This has been shown in Eq. (A.5) derived in [41,42].

$$\dot{m}_f' = -\rho^* (\underline{A}^{-1}(u))^* (\nabla p^{n+1}) + u^* \psi^n p^{n+1}$$
(A.5)

The first term in Eq. (A.5) is a diffusion-like term, which is proportional to the pressure gradient, and the second term is a convection-like term which is proportional to the absolute value of the pressure and the velocity. Upon normalizing with $u^*\psi^n$, and using the definition of the compressibility ($\psi = \rho/p = \gamma/c^2$) where γ is the ratio of specific heats, the coefficient of the pressure gradient in the diffusion term becomes proportional to the M^{-2} and that of the convection term is of order

1. At low Mach numbers, this causes the diffusion term to dominate over the convection term, making the equation elliptic. But at higher Mach numbers, the convection term dominates rendering the equation its hyperbolic nature. Further details of this formulation are described well in Refs. [40,42].

References

- [1] Y. Ju, W. Sun, Plasma assisted combustion: Dynamics and chemistry, Prog. Energy Combust. Sci. 48 (2015) 21–83.
- [2] N. Popov, Fast gas heating in a nitrogen-oxygen discharge plasma: I. Kinetic mechanism, J. Phys. D: Appl. Phys. 44 (28) (2011) 285201.
- [3] D.Z. Pai, D.A. Lacoste, C.O. Laux, Transitions between Corona, glow, and spark regimes of nanosecond repetitively pulsed discharges in air at atmospheric pressure, J. Appl. Phys. 107 (2010) 093303.
- [4] J.K. Lefkowitz, T. Ombrello, An exploration of inter-pulse coupling in nanosecond pulsed high frequency discharge ignition, Combust. Flame 180 (2017) 136–147.
- [5] J.K. Lefkowitz, T. Ombrello, Reduction of flame development time in nanosecond pulsed high frequency discharge ignition of flowing mixtures, Combust. Flame 193 (2018) 471–480.
- [6] J.K. Lefkowitz, S.D. Hammack, C.D. Carter, T.M. Ombrello, Elevated OH production from NPHFD and its effect on ignition, Proc. Combust. Inst. 38 (4) (2021) 6671–6678.
- [7] S. Adams, J. Miles, T. Ombrello, R. Brayfield, J. Lefkowitz, The effect of inter-pulse coupling on gas temperature in nanosecond-pulsed high-frequency discharges, J. Phys. D: Appl. Phys. 52 (35) (2019) 355203.
- [8] S. Shen, I. Laso, N. Rozin, J.K. Lefkowitz, On pulse energy and energy distribution for ignition of flowing mixtures, Proc. Combust. Inst. 39 (4) (2023) 5487–5498.
- [9] A. Flitti, S. Pancheshnyi, Gas heating in fast pulsed discharges in N₂-O₂ mixtures, Eur. Phys. J. - Appl. Phys. 45 (2009).
- [10] J.K. Lefkowitz, P. Guo, A. Rousso, Y. Ju, Species and temperature measurements of methane oxidation in a nanosecond repetitively pulsed discharge, Phil. Trans. R. Soc. A 373 (2015) 20140333.
- [11] N. Deak, A. Bellemans, F. Bisetti, Plasma-assisted ignition of methane/air and ethylene/air mixtures: Efficiency at low and high pressures, Proc. Combust. Inst. 38 (4) (2021) 6551–6558.
- [12] T.S. Taneja, P.N. Johnson, S. Yang, Nanosecond pulsed plasma assisted combustion of ammonia-air mixtures: Effects on ignition delays and NOx emission, Combust. Flame 245 (2022) 112327.
- [13] P.N. Johnson, T.S. Taneja, S. Yang, Plasma-based global pathway analysis to understand the chemical kinetics of plasma-assisted combustion and fuel reforming, Combust. Flame 255 (2023) 112927.
- [14] S. Yang, X. Gao, V. Yang, W. Sun, S. Nagaraja, J.K. Lefkowitz, Y. Ju, Nanosecond pulsed plasma activated C₂H₄/O₂/Ar mixtures in a flow reactor, J. Propuls. Power (2016) 1240–1252.
- [15] H. Sitaraman, R. Grout, Premixed combustion simulations with a self-consistent plasma model for initiation, in: 54th AIAA Aerospace Sciences Meeting, 2016, p. 2158.
- [16] T.S. Taneja, S. Yang, H. Sitaraman, 1D simulation of avalanche to streamer to spark transition of plasma discharge in ammonia-air combustion, in: AIAA Scitech 2024 Forum, 2024, p. 2607.
- [17] S. Kobayashi, Z. Bonaventura, F. Tholin, N.A. Popov, A. Bourdon, Study of nanosecond discharges in H₂-air mixtures at atmospheric pressure for plasma assisted combustion applications, Plasma Sources Sci. Technol. 26 (7) (2017) 075004
- [18] A.D. Gomez, N. Deak, F. Bisetti, Jacobian-free Newton-Krylov method for the simulation of non-thermal plasma discharges with high-order time integration and physics-based preconditioning, J. Comput. Phys. 480 (2023) 112007.
- [19] T.Y. Chen, T.S. Taneja, A.C. Rousso, S. Yang, E. Kolemen, Y. Ju, Time-resolved in situ measurements and predictions of plasma-assisted methane reforming in a nanosecond-pulsed discharge, Proc. Combust. Inst. 38 (2021) 6533–6540.
- [20] A. Rousso, S. Yang, J. Lefkowitz, W. Sun, Y. Ju, Low temperature oxidation and pyrolysis of n-heptane in nanosecond-pulsed plasma discharges, Proc. Combust. Inst. 36 (2017) 4105–4112.
- [21] M. Castela, B. Fiorina, A. Coussement, O. Gicquel, N. Darabiha, C.O. Laux, Modelling the impact of non-equilibrium discharges on reactive mixtures for simulations of plasma-assisted ignition in turbulent flows, Combust. Flame 166 (2016) 133–147.
- [22] T.S. Taneja, S. Yang, Numerical modeling of plasma assisted pyrolysis and combustion of ammonia, in: AIAA Scitech 2021 Forum, 2021, p. 1972.
- [23] M. Castela, S. Stepanyan, B. Fiorina, A. Coussement, O. Gicquel, N. Darabiha, C.O. Laux, A 3-D DNS and experimental study of the effect of the recirculating flow pattern inside a reactive kernel produced by nanosecond plasma discharges in a methane-air mixture, Proc. Combust. Inst. 36 (3) (2017) 4095–4103.
- [24] T.S. Taneja, T. Ombrello, J. Lefkowitz, S. Yang, Numerical investigation of ignition kernel development with nanosecond pulsed plasma in quiescent and flowing mixtures, in: AIAA SCITECH 2023 Forum, 2023, p. 0749.

- [25] Y. Bechane, B. Fiorina, A numerical investigation of plasma-assisted ignition by a burst of nanosecond repetitively pulsed discharges, Combust. Flame 259 (2024) 113106
- [26] D. Zhou, H. Zhang, S. Yang, A robust reacting flow solver with computational diagnostics based on OpenFOAM and Cantera, Aerospace 9 (2) (2022) 102.
- [27] T.S. Taneja, S. Yang, Comparing low-mach and fully-compressible CFD solvers for phenomenological modeling of nanosecond pulsed plasma discharges with and without turbulence, in: AIAA SCITECH 2022 Forum, 2022, p. 0976.
- [28] H. Jasak, OpenFOAM: Open source CFD in research and industry, Int. J. Nav. Archit. 1 (2) (2009) 89–94.
- [29] J.O. Hirschfelder, C.F. Curtiss, R.B. Bird, The Molecular Theory of Gases and Liquids, John Wiley & Sons, 1964.
- [30] L. Landau, Theory of sound dispersion, Physikalische zeitschrift der Sowjetunion 10 (1936) 34–43.
- [31] R.C. Millikan, D.R. White, Systematics of vibrational relaxation, J. Chem. Phys. 39 (1963) 3209–3213.
- [32] R.I. Issa, Solution of the implicitly discretised fluid flow equations by operator-splitting, J. Comput. Phys. 62 (1) (1986) 40–65.
- [33] A. Scotti, C. Meneveau, D.K. Lilly, Generalized smagorinsky model for anisotropic grids, Phys. Fluids A: Fluid Dyn. 5 (9) (1993) 2306–2308.
- [34] A. Bhave, M. Kraft, Partially stirred reactor model: Analytical solutions and numerical convergence study of a PDF/Monte Carlo method, SIAM J. Sci. Comput. 25 (5) (2004) 1798–1823.

- [35] T. Lu, C.K. Law, A criterion based on computational singular perturbation for the identification of quasi steady state species: A reduced mechanism for methane oxidation with NO chemistry, Combust. Flame 154 (4) (2008) 761–774.
- [36] E. Goos, A. Burcat, B. Ruscic, Extended Third Millennium Ideal Gas and Condensed Phase Thermochemical Database for Combustion with Updates from Active Thermochemical Tables, Elke Goos, Remchingen, Germany, 2010, (Accessed 19 Sept 2016).
- [37] F. Menter, Zonal two equation kw turbulence models for aerodynamic flows, in: 23rd Fluid Dynamics, Plasmadynamics, and Lasers Conference, 1993, p. 2906.
- [38] D.G. Goodwin, R.L. Speth, H.K. Moffat, B.W. Weber, Cantera: An object-oriented software toolkit for chemical kinetics, thermodynamics, and transport processes, 2021, http://dx.doi.org/10.5281/zenodo.4527812, Version 2.5.1, https://www. cantera.org.
- [39] D. Zhou, S. Yang, A robust reacting flow solver with detailed transport, chemistry, and steady-state preserving splitting schemes based on OpenFOAM and Cantera, in: AIAA Scitech 2020 Forum, 2020, p. 2139.
- [40] F. Moukalled, M. Darwish, A unified formulation of the segregated class of algorithms for fluid flow at all speeds, Numer. Heat Tr. B - Fund. 37 (1) (2000) 103–139.
- [41] I. Demirdžić, R. Issa, Ž. Lilek, Solution method for viscous flows at all speeds in complex domains, in: Proceedings of the Eighth GAMM-Conference on Numerical Methods in Fluid Mechanics, Springer, 1990, pp. 89–98.
- [42] I. Demirdžić, Ž. Lilek, M. Perić, A collocated finite volume method for predicting flows at all speeds, Internat. J. Numer. Methods Fluids 16 (12) (1993) 1029–1050.